Applied Physics Letters

Enhanced response of bulk heterojunction polymer photodetectors upon incorporating CsPbBr₃ quantum dots F

Zhongyuan Ren, Ying Su, Shaoqing Chen, Jiantao Wang iD, Changhao Wang, Changchun Wang iD, Pengfei Ma, Fanxu Meng iD, Qinghui Zeng, and Hsing-lin Wang

COLLECTIONS

F   This paper was selected as Featured

View Online   Export Citation   CrossMark

ARTICLES YOU MAY BE INTERESTED IN

Measurement of ultrafast dynamics of photoexcited carriers in β-Ga₂O₃ by two-color optical pump-probe spectroscopy
Applied Physics Letters 113, 252102 (2018); https://doi.org/10.1063/1.5058164

Measuring temperature-dependent thermal diffuse scattering using scanning transmission electron microscopy
Applied Physics Letters 113, 253101 (2018); https://doi.org/10.1063/1.5066111

Pulsed-laser deposition of InSe thin films for the detection of thickness-dependent bandgap modification
Applied Physics Letters 113, 253501 (2018); https://doi.org/10.1063/1.5064736

Enhanced response of bulk heterojunction polymer photodetectors upon incorporating CsPbBr₃ quantum dots

Zhongyuan Ren,[1,2,a)] Ying Su,[2,a)] Shaoqing Chen,[3] Jiantao Wang,[3] Changhao Wang,[1] Changchun Wang,[1] Pengfei Ma,[1] Fanxu Meng,[1,3,b)] Qinghui Zeng,[2,b)] and Hsing-lin Wang[3,b)]

[1]Jilin Institute of Chemical Technology, Chengde Street 45, Jilin 132022, People's Republic of China
[2]State Key Laboratory of Luminescence and Applications, Changchun Institute of Optics, Fine Mechanics and Physics, Chinese Academy of Sciences, Dong Nanhu Road 3888, Changchun 130033, People's Republic of China
[3]Department of Materials Science and Engineering, Southern University of Science and Technology, Shenzhen, Guangdong Province 518055, People's Republic of China

CsPbBr₃ quantum dots (QDs) were doped into a blend of poly(3-hexylthiophene) and indene-C₆₀ bisadduct to fabricate bulk heterojunction polymer photodetectors. The addition of the QDs significantly increased the shunt resistance of the device, thereby suppressing the reverse leakage current and improving both the signal-to-noise ratio and the specific detectivity. The photoresponse and recovery time both decreased because of the enhanced built-in electric field and improved charge carrier mobility. *Published by AIP Publishing.* https://doi.org/10.1063/1.5050253

The low cost, solution-processability, flexibility, and structural diversity of polymer materials[1] mean that polymer photodetectors (PPDs) have excellent potential in the fields of image sensing, communications, environmental monitoring, remote control, and chemical or biological sensing.[2–4] The photoresponse of PPDs is determined mainly by conjugated polymer donors, of which poly(3-hexylthiophene) (P3HT) is now a favored member because it offers relatively good photoelectric properties.[5–7] However, its large exciton binding energy $(0.33 \sim 0.7 \, \text{eV})$[8] means that photogenerated excitons rarely dissociate into free carriers at room temperature,[8,9] which limits device performance.

Recently, colloidal quantum dots (QDs), such as ZnO, CdTe, and PbS QDs, have been integrated into P3HT-based PPDs to improve their performance.[10–12] Colloidal QDs are compatible with the solution processing used to fabricate PPDs. Also, their optoelectronic properties (e.g., bandgap and absorption edge) can be tuned to shift the detection range from the ultraviolet to the midinfrared.[13–16] Other interesting materials are the all-inorganic CsPbX_3 (X = Cl, Br, I) perovskite QDs, whose band structure can be easily tuned by controlling the mixing ratio of PbX_2 precursors with different halide atoms.[17] CsPbX_3 QDs offer the advantages of facile synthesis, almost full coverage of the visible range, narrow emission spectra, and high quantum yields.[17–20] CsPbX_3 QDs with a tunable energy band might form an expected heterojunction with conjugated polymers to facilitate the dissociation of photogenerated excitons and/or to provide another transport path for carriers, leading to improved performance. Therefore, the combination of PPDs with CsPbX_3 QDs shows significant potential for device applications.

In this letter, we demonstrate a bulk heterojunction (BHJ) PPD based on a blend of P3HT and indene-C₆₀ bisadduct (ICBA) doped with CsPbBr₃ QDs. The device performances with and without QDs are investigated and compared, and the results show that the shunt resistance of the device increases upon doping with QDs, leading to a lower leakage current. As a result, the dark-current density of the device is suppressed by almost one order of magnitude, and the specific detectivity D^* is doubled at 520 nm and -0.2 V bias. The photoresponse and recovery time improve significantly compared with the control device without QDs, which we attribute to the higher built-in potential and charge carrier mobility induced by the QDs in the BHJ. Finally, the external quantum efficiency and responsivity also increase slightly.

The devices were fabricated in the stacking arrangement of indium tin oxide (ITO)/titanium dioxide (TiO₂)/P3HT:ICBA:CsPbBr₃ QDs/tungsten oxide (WO₃)/silver (Ag). WO₃, with a high work function of $-4.8 \, \text{eV}$,[21] enhances hole collection at the photoactive-layer–Ag interface, and the TiO₂ film on the ITO surface serves as an electron-selective layer. Patterned ITO-glass substrates were sonicated in sequence with acetone, isopropyl alcohol, and deionized water for 15 min each. The TiO₂ thin films were fabricated by using the sol-gel method, as described in Ref. 21. For the active layer, the toluene solution composed of P3HT (15 mg/ml), ICBA (15 mg/ml), and CsPbBr₃ (x mg/mL, $x = 0$, 4) was spun cast in air at 1000 rpm on top of the TiO₂ layer. P3HT and ICBA were purchased from Lumtec Corp. and used without further purification, and CsPbBr₃ QDs dispersed in toluene at a concentration of 10 mg/ml were synthesized by the Zeng group.[17] The samples were then annealed in low vacuum (vacuum oven) at $110 \, ^\circ\text{C}$ for 20 min. Finally, the devices were completed by thermal evaporation of a film of WO₃ (10 nm) and a Ag electrode. The active area of the photodetector was about $0.06 \, \text{cm}^2$.

The CsPbBr₃ QD morphology was investigated by using high-resolution transmission electron microscopy (HR-TEM, FEI, Talos F200X). In addition, a cross-sectional image of the device was acquired by using field emission scanning electron microscopy (FE-SEM, TESCAN, MIRA3), and the QD distribution in the active layer was verified by

[a)]Z. Ren and Y. Su contributed equally to this work.
[b)]Authors to whom correspondence should be addressed: fxmengjlu@gmail.com; qhzeng@ciomp.ac.cn; and wangxl3@sustc.edu.cn

energy-dispersive x-ray spectroscopy (EDS, Oxford Instrument, X-Max^N) mapping of Pb and Br. Absorption and photoluminescence (PL) spectra were measured at indoor temperatures by using a Shimadzu UV-1800 spectrophotometer and a Hitachi F-7000 fluorescence spectrofluorimeter, respectively. The current-density–voltage (*J-V*) characteristics and the responsivity of the PPDs were measured by using a computer-programmed Keithley 2400 source meter. A 100 W xenon lamp and a monochromator with a filter wheel provided a source of monochromatic light. The intensity of the monochromatic light was calibrated by using a standard silicon photodetector (Zolix, QE-B1). The 100 W xenon lamp was chopped by using a chopper wheel and the response time was determined with the aid of a digital oscilloscope.

TEM and HR-TEM images of CsPbBr$_3$ QDs are shown in Figs. 1(a) and 1(b), respectively. The as-prepared CsPbBr$_3$ QDs are estimated to have an average size of ∼20 nm and a cubic shape, which is determined by the perovskite crystal structure [Fig. 1(a)]. The QD structure is further confirmed by the lattice fringes of 0.58 nm shown in Fig. 1(b), which correspond to the (100) plane of cubic phase CsPbBr$_3$.[22] The device architecture is shown schematically in Fig. 1(c), and the cross-sectional FE-SEM image of the device [Fig. 1(d)] shows that the ITO/TiO$_2$, active layer, and WO$_3$/Ag film are about 200, 110, and 80 nm thick, respectively. In addition, the EDS mapping of Pb and Br in the active layer (Fig. S1) reveals an almost homogeneous distribution of QDs throughout the active layer.

The absorption spectra in Fig. 2(a) are almost the same for the active layers with and without QDs at wavelengths below 460 nm. This phenomenon may be attributed to the strong absorption of high-energy photons at or near the surface of the BHJ film. For longer wavelengths, the incident light can travel into the active layer, and the absorption of the active layer can be strengthened by doping it with CsPbBr$_3$ QDs, which have an absorption edge of ∼528 nm.
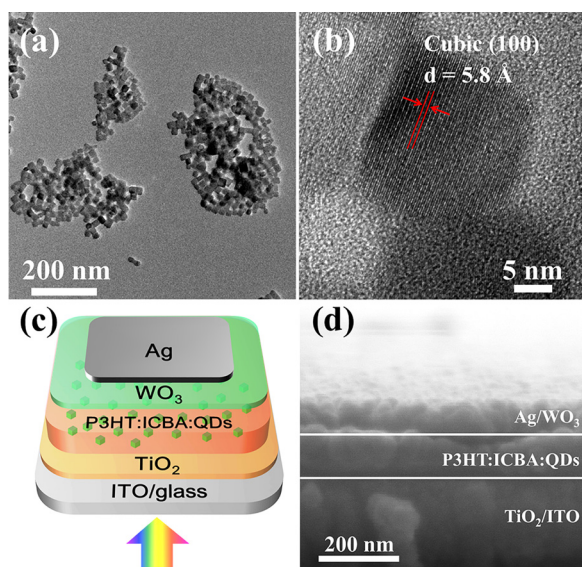

FIG. 1. (a) TEM and (b) HR-TEM images of CsPbBr$_3$ QDs. (c) Device structure of the PPDs with CsPbBr$_3$ QDs. (d) Cross-sectional FE-SEM image of the device.
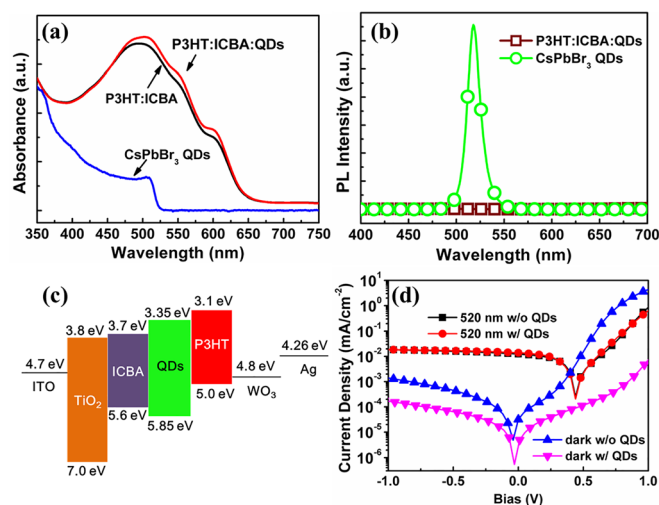

FIG. 2. (a) Absorption spectra of as-prepared CsPbBr$_3$ QDs and active layers with and without QDs. (b) PL spectra of as-prepared QDs and BHJ film with QDs. (c) Energy-level scheme of materials involved in the BHJ PPDs. (d) *J-V* characteristics of devices with and without QDs in the dark and under illumination at the wavelength of 520 nm with an irradiation-intensity of 51.8 μW/cm^2.

Nevertheless, an apparent PL quenching occurs in the active layer with QDs compared with the as-prepared QDs [Fig. 2(b)]. This quenching implies the formation of another transport channel for carriers, which would hinder the radiative recombination of photogenerated excitons in the QDs. In addition, the energy-level diagram in Fig. 2(c)[19,20,23] suggests that the photogenerated excitons in both P3HT and QDs might separate into free holes and electrons at the P3HT/QD interfaces. In this case, the electrons would transfer from the QD conduction band (E$_{CB}$) to the lowest unoccupied molecular orbital (LUMO) level of ICBA or to the conduction band of TiO$_2$, before finally being collected by the ITO electrode. Correspondingly, the holes would move to the highest occupied molecular orbital (HOMO) level of P3HT and from there eventually be driven to the Ag electrode.

Figure 2(d) shows the *J-V* characteristics of devices with and without QDs and measured in the dark and under illumination at 520 nm with an irradiation intensity of 51.8 μW/cm^2. Under reverse bias, the dark-current density J_d of the sample device with QDs is one order of magnitude less than that of the control device without QDs, which means a significant decrease in reverse leakage current. The decreased reverse leakage current can be ascribed to the dramatic increase in shunt resistance R_{sh} from ∼6216.2 to ∼11 461.3 Ω cm^2 upon adding QDs, where R_{sh} is defined by the slope of the *J-V* curves near 0 V under illumination. A more detailed discussion is provided in the supplementary material. In addition, the higher built-in potential in QD-doped BHJs can be anticipated from the energy level alignment in Fig. 2(c), and direct evidence of this is given by the higher forward-bias shift of the diffusion-current-dominated regime of the dark *J-V* curve.

Under illumination at 520 nm, the photocurrent density $J_{ph} = 13.92$ μA/cm^2 of the sample device is slightly greater than the 12.49 μA/cm^2 of the control device in the short-circuit mode (at 0 V bias), evincing the benefits of QDs for the absorption of incident light and exciton dissociation. However, the photocurrent density gradually becomes equal

to that of the control device upon further increasing the reverse bias. This trend might result from the saturation of photogenerated carriers extracted by the electrodes under a high internal electric field and low illumination density. To investigate the variation in charge carrier mobility, the space-charge-limited current of the devices was measured with and without QDs. The structure of the electron-only and hole-only devices was ITO/TiO$_2$/BHJ/Bathocuproine (BCP)/Ag and ITO/poly(3,4-ethylenedioxythiophene):polystyrene sulfonate/BHJ/WO$_3$/Ag, respectively. Figure S3 shows that the current density in devices with QDs exceeds that of devices without QDs in both electron-only and hole-only devices. Upon introducing the QDs, the calculated electron mobility in the BHJ film increases from $\sim 2.62 \times 10^{-2}$ to $\sim 7.35 \times 10^{-2}$ cm^2 V^{-1} s^{-1}, and the hole mobility in the BHJ film improves by about one order of magnitude from $\sim 2.0 \times 10^{-4}$ to $\sim 2.22 \times 10^{-3}$ cm^2 V^{-1} s^{-1}. These results also support our deduction of the formation of another transport channel for carriers, which contributes to a higher photocurrent at zero bias.

One of the most critical parameters of photodetectors is the signal-to-noise ratio (J_{ph}/J_d), which is 687 at -0.2 V bias for the sample device versus 118 for the control device (Table S1). The signal-to-noise ratio J_{ph}/J_d of both devices reaches a maximum of about 26 000 (with QDs) and 2659 (without QDs) at -0.04 V due to the ultralow dark current, which indicates poor charge injection from the contacts.[24]

We also investigate the spectral photoresponse of these devices at various bias levels [see Figs. 3(a) and 3(b)]. The results show that the responsivity of the sample device is better than that of the control device over a wide band of 380~640 nm for a bias below -1 V, and the responsivity of both devices is almost the same at -1 V bias because of the previously mentioned saturation of extracted photogenerated carriers. As shown in Table S3, the responsivity of the QD-doped BHJ photodetectors is similar to that of commercial silicon photodiodes, but not as high as that reported for CsPbX_3 QD detectors with a phototransistor structure. However, a trade-off between responsivity and response speed is usually involved (a phototransistor has higher responsivity, whereas a photodiode has a faster response).[25] The variation in the external quantum efficiency spectrum, which is derived from the spectral photoresponse,[10] is similar to the variation in the spectral responsivity, shown in Fig. S4. The specific detectivity D^* is determined by J_d and the spectral photoresponse,[25] and the detectivity spectra of PPDs without and with QDs are shown in Figs. 3(c) and 3(d), respectively. Benefiting from the inhibited dark current, the specific detectivity D^* of the sample device increases to over twice that of the control device, as shown in Table S2. The highest D^* of 2.04×10^{13} Jones occurs at zero bias for the PPD with CsPbBr$_3$ QDs, proving the excellent self-power ability.

Figure 4 shows the time response of the devices to switching the light on and off. The response time of the device is obtained by measuring the voltage variation of a 1 MΩ load resistance in the test circuit. The rise time τ_r is 860 μs for the control device and 520 μs for the sample device. The fall time τ_d decreases from 3.62 ms in the control device to 2.28 ms in the sample device. The faster response of the
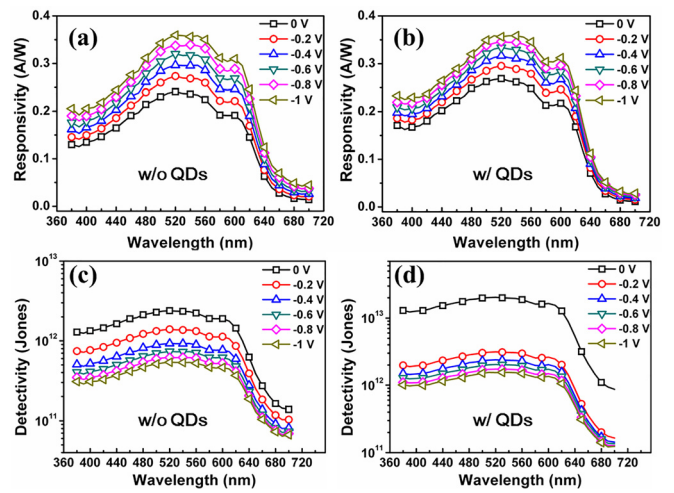

FIG. 3. Responsivity and detectivity spectra of (a) and (c) control device and (b) and (d) sample device, respectively.
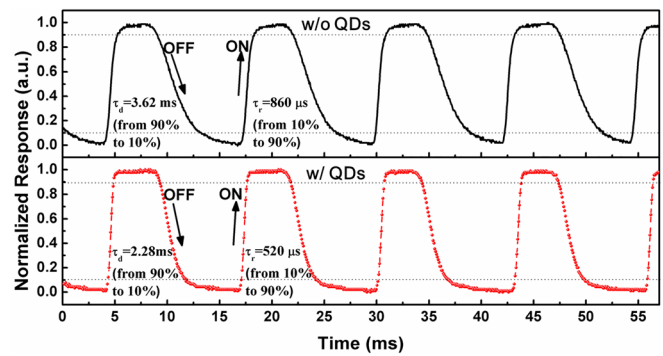

FIG. 4. Time response of control and sample devices.

sample device is attributed to the reinforced built-in potential and improved charge carrier mobility arising from the addition of QDs in the active layer, which allows the carriers to travel across the BHJ film with a higher drift velocity. The measured rise time and fall time of our devices are relatively fast compared with those reported for other CsPbX_3 QD detectors (see Table S3), although they remain slower than commercial detectors, which operate on the nanosecond or picosecond timescale. In addition, the voltage can be reproducibly switched from the "on" state to the "off" state by periodically turning the light on and off, indicating outstanding stability.

In summary, we demonstrate herein a low dark current and a quick response from bulk heterojunction polymer photodetectors by incorporating CsPbBr$_3$ QDs into a P3HT:ICBA blend. The shunt resistance of the device increases significantly, which suppresses the reverse leakage current and leads to a very high D^* of 2.04×10^{13} Jones and a J_{ph}/J_d of 26 000 at zero bias for the QD-doped devices illuminated at 520 nm. The built-in potential is also elevated due to the QD-induced change in energy-level alignment in the BHJ film. Because the increase in both built-in potential and charge carrier mobility facilitates photoinduced charge dissociation and transport in the active layer, the photoresponse and recovery time of the devices are shortened from 860 to 520 μs and from 3.62 to 2.28 ms, respectively.

See supplementary material for the EDS mapping of Pb and Br in the active layer (supplementary Fig. S1), a summary of the performance data of the control and sample devices (supplementary Tables S1 and S2), a discussion of the reduced dark current based on an equivalent circuit for a photodiode (supplementary Fig. S2), measurements of the space-charge-limited current in the devices with and without QDs (supplementary Fig. S3), the external quantum efficiency spectra of the devices (supplementary Fig. S4), and performance comparisons of photodetectors from previous reports based on CsPbX_3 QDs and commercial silicon photodiodes (supplementary Table S3).

[1]S. Tong, J. Yuan, C. Zhang, C. Wang, B. Liu, J. Shen, H. Xia, Y. Zou, H. Xie, J. Sun, S. Xiao, J. He, Y. Gao, and J. Yang, npj Flexible Electron. **2**, 7 (2018).

[2]X. Gong, M. Tong, Y. Xia, W. Cai, J. S. Moon, Y. Cao, G. Yu, C. L. Shieh, B. Nilsson, and A. J. Heeger, Science **325**, 1665 (2009).

[3]X. Wang, O. Hofmann, R. Das, E. M. Barrett, A. J. Demello, J. C. Demello, and D. D. Bradley, Lab Chip **7**, 58 (2007).

[4]T. Agostinelli, M. Campoyquiles, J. C. Blakesley, R. Speller, D. D. C. Bradley, and J. Nelson, Appl. Phys. Lett. **93**, 203305 (2008).

[5]T. Wang, Y. Wang, L. Zhu, L. Lv, Y. Hu, Z. Deng, Q. Cui, Z. Lou, Y. Hou, and F. Teng, Org. Electron. **56**, 51 (2018).

[6]B. Ouyang, K. Zhang, and Y. Yang, Adv. Mater. Technol. **2**, 1700208 (2017).

[7]H. Wang, S. Xing, Y. Zheng, J. Kong, J. Yu, and A. D. Taylor, ACS Appl. Mater. Interfaces **10**, 3856 (2018).

[8]R. S. Bhatta and M. Tsige, Polymer **55**, 2667 (2014).

[9]S. Guenes, H. Neugebauer, and N. S. Sariciftci, Chem. Rev. **107**, 1324 (2007).

[10]L. Shen, Y. Fang, H. Wei, Y. Yuan, and J. Huang, Adv. Mater. **28**, 2043 (2016).

[11]H. Zhang, Y. Zhang, X. Song, Y. Yu, M. Cao, Y. Che, Z. Zhang, H. Dai, J. Yang, and G. Zhang, ACS Photonics **4**, 584 (2017).

[12]R. Dong, C. Bi, Q. Dong, F. Guo, Y. Yuan, Y. Fang, Z. Xiao, and J. Huang, Adv. Opt. Mater. **2**, 549 (2014).

[13]I. Moreels, K. Lambert, D. Smeets, D. D. Muynck, T. Nollet, J. C. Martins, F. Vanhaecke, A. Vantomme, C. Delerue, and G. Allan, ACS Nano **3**, 3023 (2009).

[14]E. J. D. Klem, D. D. Macneil, P. W. Cyr, L. Levina, and E. H. Sargent, Appl. Phys. Lett. **90**, 183113 (2007).

[15]N. Zhao, T. P. Osedach, L. Y. Chang, S. M. Geyer, D. Wanger, M. T. Binda, A. C. Arango, M. G. Bawendi, and V. Bulovic, ACS Nano **4**, 3743 (2010).

[16]Z. Ni, L. Ma, S. Du, Y. Xu, M. Yuan, H. Fang, Z. Wang, M. Xu, D. Li, and J. Yang, ACS Nano **11**, 9854 (2017).

[17]Y. Su, X. Chen, W. Ji, Q. Zeng, Z. Ren, Z. Su, and L. Liu, ACS Appl. Mater. Interfaces **9**, 33020 (2017).

[18]J. Li, L. Xu, T. Wang, J. Song, J. Chen, J. Xue, Y. Dong, B. Cai, Q. Shan, and B. Han, Adv. Mater. **29**, 1603885 (2017).

[19]H. Li, X. Zheng, Y. Liu, Z. Zhang, and T. Jiang, Nanoscale **10**, 1650 (2018).

[20]V. K. Ravi, G. B. Markad, and A. Nag, ACS Energy Lett. **1**, 665 (2016).

[21]C. Tao, S. Ruan, G. Xie, X. Kong, L. Shen, F. Meng, C. Liu, X. Zhang, W. Dong, and W. Chen, Appl. Phys. Lett. **94**, 043311 (2009).

[22]Y. Shang, G. Li, W. Liu, and Z. Ning, Adv. Funct. Mater. **28**, 1801193 (2018).

[23]H. Xin, S. Subramaniyan, T.-W. Kwon, S. Shoaee, J. R. Durrant, and S. A. Jenekhe, Chem. Mater. **24**, 1995 (2012).

[24]F. Meng, L. Shen, Y. Wang, S. Wen, X. Gu, J. Zhou, S. Tian, and S. Ruan, RSC Adv. **3**, 21413 (2013).

[25]H. Wang and D. H. Kim, Chem. Soc. Rev. **46**, 5204 (2017).